INTERNATIONAL JOURNAL FOR NUMERICAL METHODS IN FLUIDS, VOL. 20, 135–155 (1995)

A EULERIAN/LAGRANGIAN MODEL TO CALCULATE THE EVOLUTION OF A WATER DROPLET SPRAY

PAUL CREISMEAS

DGA/CEPr, Saclay, F-91895 Orsay Cedex, France

SUMMARY

We introduce a Eulerian/Lagrangian model to compute the evolution of a spray of water droplets inside a complex geometry. To take into account the complex geometry we define a rectangular mesh and we relate each mesh node to a node function which depends on the location of the node. The time-dependent incompressible and turbulent Navier–Stokes equations are solved using a projection method. The droplets are regarded as individual entities and we use a Lagrangian approach to compute the evolution of the spray. We establish the exchange laws related to mass and heat transfer for a droplet by introducing a mass transfer coefficient and a heat transfer coefficient. The numerical results from our model are compared with those from the literature in the case of a falling droplet in the atmosphere and from experimental investigation in a wind tunnel in the case of a polydisperse spray. The comparison is fairly good. We present the computation of a water droplet spray inside a complex and realistic geometry and determine the characteristics of the spray in the vicinity of obstacles.

KEY WORDS Diphasic flow Eulerian/Lagrangian model Complex geometry Projection method Navier–Stokes equations

1. INTRODUCTION

Many practical problems involve fluid flows containing droplets. These problems range from fuel combustion and evaporation[1–6] to the evolution of subcooled water droplets in the open air.[7–10] In this paper we are interested in problems concerning the evolution of a water spray inside a complex geometry. Two fundamentally different[11] approaches exist to describe such flows: the first approach, which is usually termed the 'Eulerian/Eulerian' method or 'two-fluid model', considers the droplet spray as a continuous phase; the second approach, called the 'Eulerian/Lagrangian' method, considers the spray as a discrete phase. The main advantages of the former method seem to be its great computational efficiency to resolve monodisperse flows[12–14] and the possibility to take into account the coupling of the two phases. However, if the diphasic flow is a polydisperse one, the latter method is more appropriate. The Eulerian/Lagrangian method is also a powerful and efficient tool for the analysis of droplet impacts.[15] A quite popular method to take into account the turbulence is the 'Monte Carlo' method.[16,17] However, it can be shown in the case of non-homogeneous and non-isotropic turbulence, e.g. in a mixing area or behind an obstacle, that small-scale turbulent diffusion can be neglected compared with large-scale turbulent dispersion.[18,19]

The water spray generated by nozzles is not generally a monodisperse spray. In our case the droplets range from around 5 to 100 μm, so we choose a Eulerian/Lagrangian method to describe the evolution of the water spray. This choice allows droplets to retain their individual

CCC 0271–2091/95/020135–21

Received May 1993
Revised August 1994

characteristics and avoids the problem of numerical diffusion.[20] Each computational droplet represents a class of droplets possessing the same size. To be representative, the computation requires a large number of droplets, but our experience shows that this number need not to be too excessive. The ratio of total mass of water injected to that of air is small, so we can consider the two phases to be uncoupled. However, the problem is not reduced to the calculation of trajectories in a known velocity field, since droplets tend to evaporate. In order to take this effect into account, we need mass transfer and heat transfer laws. Willbank and Schulz[21] introduce an analytical model to calculate the evolution of a water spray in a wind tunnel. They consider the continuous phase of the diphasic flow as an air–water vapour mixture and a coupling between droplet evaporation and thermodynamic characteristics of the continuous phase. Their results are accurate, but unfortunately the method is restricted to unidimensional and inviscid flows. The model described in this paper differs from that of Willbank and Schulz mainly in a reformulation of the exchange laws, which allows us to take into account the turbulence through correlations related to the Sherwood number for the convection and to the Nusselt number for the heat transfer; furthermore, our model takes into account multidimensional and viscous flows. We consider the continuous phase as an air flow and we neglect the influence of the evaporation of droplets on the saturation of air. We assume no interactions, no collisions and no coalescence of droplets. The only forces acting on droplets are the aerodynamic drag and gravity. The turbulence is neglected in this effect. To calculate the gas phase, we consider the 2D, time-dependent incompressible Navier–Stokes equations in terms of mean velocity and we use a mixing length model of the turbulence. Numerical results are compared with results from the literature or with data from experimental investigations. The correspondence is fairly good.

In Sections 2 and 3 we introduce the governing equations for the continuous and discrete phases. The time discretization method is presented in Section 4. In Section 5 we compare the results from our model with those of Beard and Pruppacher[9] and Pruppacher and Klett.[7] We present a numerical simulation of a droplet spray in a realistic geometry in Section 6 and we conclude in Section 7.

2. BASIC EQUATIONS FOR CONTINUOUS PHASE

We consider the time-dependent turbulent Navier–Stokes equations for an incompressible flow,

$$\frac{\partial u_i}{\partial x_i} = 0, \tag{1}$$

$$\frac{\partial u_i}{\partial t} + u_j \frac{\partial u_i}{\partial x_j} = -\frac{\partial}{\partial x_i}\frac{p}{\rho_0} + \frac{\partial}{\partial x_j}\left[\nu\left(\frac{\partial u_i}{\partial x_j} + \frac{\partial u_i}{\partial x_i}\right) - \overline{u_i' u_j'}\right], \tag{2}$$

where ρ_0 is the density and ν is the kinematic viscosity. To evaluate the Reynolds stresses, we use the Boussinesq relation

$$-\overline{u_i' u_j'} = \nu_t\left(\frac{\partial u_i}{\partial x_j} + \frac{\partial u_j}{\partial x_i}\right) - \tfrac{2}{3}\delta_{ij}k, \tag{3}$$

where ν_t is the turbulent viscosity, δ_{ij} is the Kronecker symbol and k is the kinetic energy. This term can be regarded as a 'turbulent pressure' term and can be included in the pressure terms.[22] Thus we obtain

$$\frac{\partial u_i}{\partial t} + u_j \frac{\partial u_i}{\partial x_j} = -\frac{\partial}{\partial x_i} P + \frac{\partial}{\partial x_j}[2(\nu + \nu_t)S_{ij}], \tag{4}$$

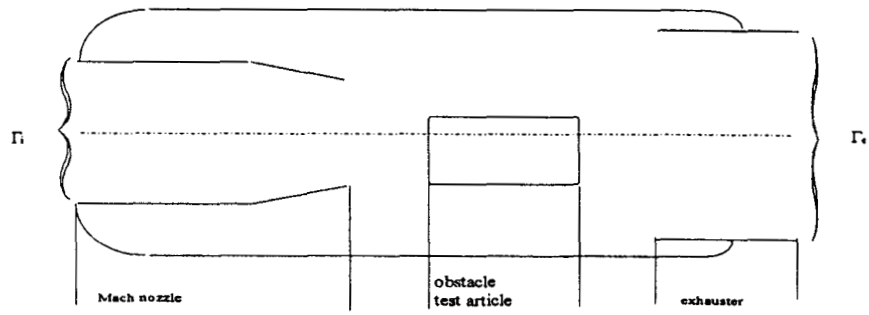

Figure 1. Computational domain

where

$$S_{ij} = \frac{1}{2}\left(\frac{\partial u_j}{\partial x_i} + \frac{\partial u_i}{\partial x_j}\right).$$

If we consider a 2D fluid flow and set $(u_1, u_2) = (u, v)$, then (1)–(4) become

$$\left(\frac{\partial u}{\partial t} + u\frac{\partial u}{\partial x} + v\frac{\partial u}{\partial y}\right) - \frac{\partial}{\partial x}\left(2(\nu + \nu_t)\frac{\partial u}{\partial x}\right) - \frac{\partial}{\partial y}\left((\nu + \nu_t)\frac{\partial u}{\partial y}\right) - \frac{\partial}{\partial y}\left((\nu + \nu_t)\frac{\partial v}{\partial x}\right) = -\frac{\partial p}{\partial x}, \quad (5)$$

$$\left(\frac{\partial v}{\partial t} + u\frac{\partial v}{\partial x} + v\frac{\partial v}{\partial y}\right) - \frac{\partial}{\partial x}\left(2(\nu + \nu_t)\frac{\partial v}{\partial x}\right) - \frac{\partial}{\partial y}\left((\nu + \nu_t)\frac{\partial v}{\partial y}\right) - \frac{\partial}{\partial x}\left((\nu + \nu_t)\frac{\partial u}{\partial y}\right) = -\frac{\partial p}{\partial y}, \quad (6)$$

$$\frac{\partial u}{\partial x} + \frac{\partial v}{\partial y} = 0. \quad (7)$$

To calculate ν_t, we use the Smagorinksy model[23]

$$\nu_t = \frac{1}{\rho_0}(c_s\,\Delta x\,\Delta y)^2\sqrt{\left[\frac{1}{2}\left(\frac{\partial u}{\partial y} + \frac{\partial v}{\partial x}\right)^2\right]}, \quad (8)$$

where Δx and Δy are the mesh sizes in directions x and y respectively and c_s is a constant of order 0·1.

If $\partial\Omega$ is the limit of the computational domain, we can write $\partial\Omega = \Gamma_i \cup \Gamma_e \cup \Gamma \cup \Gamma_{obst}$, where Γ_i and Γ_e are the entrance and exit sections of the flow respectively, Γ represents the upper and lower walls and Γ_{obst} is the limit of the obstacles (Figure 1). The boundary conditions for the velocity $\vec{u}_{\partial\Omega}$ are a no-slip condition on Γ and Γ_{obst} (i.e. $\vec{u}_\Gamma = 0$ and $\vec{u}_{\Gamma_{obst}} = 0$), a given $\vec{u}_{\partial\Omega}$ on Γ_i and a free exit condition on Γ_e.

3. BASIC EQUATIONS FOR DISCRETE PHASE

3.1. Assumptions

Heat diffusion and species diffusion obey a Fourier law. We consider that the liquid/vapour interface is in thermodynamic equilibrium, so the pressure over the surface of droplets is equal to the saturation vapour pressure. We neglect droplet coalescence and droplet collision effects and the only forces taken into account to calculate droplet trajectories are the aerodynamic drag and gravity. The turbulence is neglected for droplet trajectories but is taken into account for droplet heat and mass exchanges through correlations related to the Sherwood number for

the convection and to the Nusselt number for the heat transfer. The discrete and continuous phases are uncoupled, the mixture of air and water vapour is considered to have the same behaviour as the air only and the droplets are spherical.

3.2. Mass calculation

To calculate the mass rate of exchange, we introduce a mass transfer coefficient according to Pruppacher and Klett's method,[7] i.e.

$$k_{v,\Omega} = \frac{dm_d/dt}{\Omega\rho_0(p_v - p_{v,d})/(p - p_{v,d})}. \tag{9}$$

Here ρ_0 is the density of air, $p_{v,d}$ is the pressure of water vapour at the surface of the droplet and, according to a previous assumption, also the pressure of saturation vapour at the surface of the droplet, m_d is the mass of the droplet, p is the pressure of air and p_v is the actual pressure of water vapour in the environment, which can be expressed by introducing the saturation hg as

$$p_v = hgp_{v,sat}, \tag{10}$$

where $p_{v,sat}$ is the water vapour pressure in the environment at saturation. Ω is the total area of the body concerned and is related to the perimeter p_r of its area projected in the direction of the flow by the relation[7]

$$L = \frac{\Omega}{p_r}. \tag{11}$$

In the case of a trivial geometry such as a droplet we have $L = d_d$, where d_d is the droplet diameter. By introducing Ω and p_r, we are able to extend the expression of $k_{v,\Omega}$ to complex geometries such as an ice crystal. The ventilation effect is described in terms of the Sherwood number, which depends on the characteristic length L according to[7]

$$Sh_d = \frac{k_{v,\Omega}L}{D_v}, \tag{12}$$

where D_v is the diffusivity water vapour in air. Equations (9) and (12) give us

$$\frac{dm_d}{dt} = \frac{\Omega}{L} Sh_d D_v \rho_0 \frac{hgp_{v,sat} - p_{v,d}}{p - p_{v,d}}. \tag{13}$$

For a droplet we have $\Omega/L = \pi d_d$. We introduce the molar proportion of water vapour in the environment as

$$x_v = \frac{hgp_{v,sat}}{p} \tag{14}$$

and the molar proportion of water vapour at the surface of the droplet as

$$x_{vs} = \frac{p_{v,d}}{p}. \tag{15}$$

Then, using (14) and (15), equation (13) can be recast as

$$\frac{dm_d}{dt} = \pi d_d Sh_d D_v \rho_0 \frac{x_v - x_{vs}}{1 - x_{vs}}. \tag{16}$$

The Sherwood number is calculated as[7]

$$Sh_d = 2f_v, \tag{17}$$

where f_v is a ventilation coefficient defined as

$$f_v = \frac{dm_d/dt}{(dm_d/dt)_0}, \tag{18}$$

with the subscript '0' denoting the droplet at rest in the flow. Introducing the Reynolds number

$$Re_d = \frac{|V - V_d| d_d}{\nu}, \tag{19}$$

where V is the value of the Euclidean norm of the air velocity in the vicinity of the droplet and V_d is the Euclidean norm of the droplet velocity, and the Schmidt number

$$Sc_d = \frac{\nu}{D_v}, \tag{20}$$

we have[9]

$$f_v = 1 + 0{\cdot}108 Sc_d^{1/3} Re_d^{1/2} \quad \text{if } (Sc_d^{1/3} Re_d^{1/2})^2 < 1{\cdot}4, \tag{21}$$

$$f_v = 0{\cdot}78 + 0{\cdot}308 Sc_d^{1/3} Re_d^{1/2} \quad \text{otherwise.} \tag{22}$$

3.3. Droplet surface temperature calculation

In analogy with (9) we define the heat transfer coeffficient

$$h_\Omega = \frac{dq/dt}{\Omega(T - T_d)}, \tag{23}$$

where T_d is the temperature of the droplet surface and T is the temperature of the environment. We also introduce the Nusselt number

$$Nu_d = \frac{h_\Omega L}{k}, \tag{24}$$

where L has the same definition as in (11) and k is the thermal conductivity of air. In the case of a spherical droplet we have $\Omega/L = \pi d_d$, where d_d is the droplet diameter. Hence (23) and (24) give us

$$\frac{dq}{dt} = k Nu_d \pi d_d (T - T_d). \tag{25}$$

When a droplet is placed in a environment at $T \neq T_d$, we have a heat flux from the air to the droplet if $T > T_d$ or from the droplet to the air if $T < T_d$, and this heat flux is given by expression (25). If the saturation is $hg < 1$, we also have a loss of heat by evaporation given by $-H_{vl} dm_d/dt$, where H_{vl} is the latent heat of evaporation. Thus the total rate of droplet heat evolution is expressed by

$$\left.\frac{dq}{dt}\right|_{\text{total}} = k Nu_d \pi d_d (T - T_d) + H_{vl} \frac{dm_d}{dt}. \tag{26}$$

Given the heat and mass relation

$$\left.\frac{dq}{dt}\right|_{total} = m_d c_{pl} \frac{d(T - T_d)}{dt}, \tag{27}$$

(26) becomes

$$m_d c_{pl} \frac{d(T - T_d)}{dt} = kNu_d \pi d_d (T - T_d) + H_{vl} \frac{dm_d}{dt}. \tag{28}$$

If we assume that $dT/dt \ll dT_d/dt$, we finally obtain

$$m_d c_{pl} \frac{dT_d}{dt} = KNu_d \pi d_d (T - T_d) + H_{vl} \frac{dm_d}{dt}. \tag{29}$$

The Nusselt number is calculated as[7]

$$Nu_d = 2f_h, \tag{30}$$

where f_h is a thermal ventilation coefficient defined as

$$f_h = \frac{dq/dt}{(dq/dt)_0}, \tag{31}$$

with the subscript '0' denoting the heat exchange when the droplet is at rest in the flow. To calculate f_h, we introduce the Prandtl number Pr_d for a droplet as

$$Pr_d = \frac{\mu c_p}{k}, \tag{32}$$

where μ and c_p are the viscosity and heat capacity of the gas phase respectively. Then

$$f_h = 1 + 1{\cdot}108(Re_d^{1/2} Pr_d^{1/3})^2 \quad \text{if } Re_d^{1/2} Pr_d^{1/3} < 1{\cdot}4259, \tag{33}$$

$$f_h = 0{\cdot}78 + 0{\cdot}308 Re_d^{1/2} Pr_d^{1/3} \quad \text{otherwise.} \tag{34}$$

3.4. Trajectory calculation

For a droplet the balance of forces acting on it can be set in the form

$$\frac{d\vec{q}}{dt} = \sum f_{ext}, \tag{35}$$

where

$$\vec{p} = m_d \vec{V}_d \tag{36}$$

and $\vec{V}_d$ is the instantaneous velocity of the droplet. If we consider that the only force which acts on the droplet is the aerodynamic drag, the right-hand side of equation (35) can be expressed as

$$\sum f_{ext} = \tfrac{1}{2}\rho\pi(d_d^2/4)c_x/\vec{V} - \vec{V}_d/(\vec{V} - \vec{V}_d), \tag{37}$$

where $\vec{V}$ is the air velocity in the vicinity of the droplet and c_x is the drag coefficient given by

$$c_x = \frac{24}{Re_d}(1 + 0{\cdot}15 Re_d^{0{\cdot}687}). \tag{38}$$

The droplet is assumed to be spherical, so by projecting (35) on the x-axes and y-axes, it is possible to write, setting $\vec{V} = (u, v)$ and $\vec{V}_d = (u_d, v_d)$,

$$\frac{d(m_d u_d)}{dt} = \frac{\rho\pi}{2}\frac{d_d^2}{4} c_x |u - u_d|(u - u_d), \tag{39}$$

$$\frac{d(m_d v_d)}{dt} = \frac{\rho\pi}{2}\frac{d_d^2}{4} c_x |v - v_d|(v - v_d). \tag{40}$$

4. METHOD FOR TIME DISCRETIZATION

4.1. Time discretization for gas phase

We employ a projection method first introduced by Chorin[24] and Temam[25] for laminar flows to resolve the turbulent equations (1)–(3). At time $n\Delta t$ the solution $(u, v)^{n+1}$ is decomposed on two orthogonal subspaces defined as follows

$$(u, v) \in \{L^2(\Omega)/\operatorname{div}(u, v) = 0\} \text{ inside } \Omega, \qquad (u, v) \cdot n = 0 \quad \text{on the boundary } \partial\Omega,$$

$$H^{\perp} = \operatorname{grad}(H^1(\Omega)),$$

where

$$L^2(\Omega) = \left\{(u, v)/\int_{\Omega} \|(u, v)\|_{L^2}^{\Omega}\, dx < \infty\right\}, \qquad \|(u, v)\|_{L^2} = \left(\int_{\Omega} \|(u, v)\|^2\, dx\right)^{1/2}$$

and $H^1(\Omega)$ is a first-order Sobolev space. Thus we have $L^2(\Omega) = H \oplus H^{\perp}$. We define the projection P_h: $L^2(\Omega) \to H$ and it is possible to write

$$\forall (u, v) \in L^2(\Omega) \quad \exists p \in H^{\perp}/(u, v) = P_H(u, v) + \operatorname{grad} p.$$

The principle of the projection is based on a predictor–corrector strategy. It consists of calculating a predicted velocity (u^*, v^*) so that

$$\frac{u^* - u^n}{\Delta t} + u^n \frac{\partial u^*}{\partial x} + v^n \frac{\partial u^*}{\partial y} - \frac{\partial}{\partial x}\left(2(\nu + \nu_t)\frac{\partial u^*}{\partial x}\right) - \frac{\partial}{\partial y}\left((\nu + \nu_t)\frac{\partial u^*}{\partial y}\right) - \frac{\partial}{\partial y}\left((\nu + \nu_t)\frac{\partial v^n}{\partial y}\right) = 0, \tag{41}$$

$$\frac{v^* - v^n}{\Delta t} + u^n \frac{\partial v^*}{\partial x} + v^n \frac{\partial v^*}{\partial y} - \frac{\partial}{\partial x}\left(2(\nu + \nu_t)\frac{\partial v^*}{\partial x}\right) - \frac{\partial}{\partial y}\left((\nu + \nu_t)\frac{\partial v^*}{\partial y}\right) - \frac{\partial}{\partial y}\left((\nu + \nu_t)\frac{\partial u^n}{\partial y}\right) = 0, \tag{42}$$

where $(u, v)^n$ is the velocity that has been computed at the nth step and (u^*, v^*) satisfies the correct boundary condition. Note that (u^*, v^*) does not satisfy the incompressibility condition. The velocity field (u^*, v^*) is corrected by projecting it in H. We use P_H to project (u^*, v^*) onto H and we set

$$(u, v)^{n+1} = P_H(u^*, v^*),$$

i.e.

$$(u, v)^{n+1} = (u^*, v^*) - \nabla p.$$

Thus we have

$$u^{n+1} = u^* - \frac{\partial p}{\partial x}, \tag{43}$$

$$v^{n+1} = v^* - \frac{\partial p}{\partial y}, \tag{44}$$

$$\frac{\partial u^{n+1}}{\partial x} + \frac{\partial v^{n+1}}{\partial y} = 0. \tag{45}$$

The projection method is a fractional step method which uncouples the velocity and pressure. The numerical efficiency of the scheme is obvious, since the velocity and pressure are totally uncoupled. By applying the divergence operator to (43) and (44) and using (45), we find a Poisson equation for the pressure:

$$\Delta p = \frac{\nabla \cdot (u^*, v^*)}{\Delta t}, \tag{46}$$

$$\frac{\partial p}{\partial n} = 0 \quad \text{on the boundary } \partial\Omega. \tag{47}$$

4.2. Time discretization for discrete phase

Equations (16), (29), (39) and (40) can be written in the form

$$\frac{\partial \Phi}{\partial t} = S, \tag{48}$$

where $\Phi = \{m_d;\ T_d;\ m_d u_d;\ m_d v_d\}$ and S is the second member associated with the quantity concerned. A first-order explicit scheme yields

$$\frac{\Phi^{n+1} - \Phi^n}{\Delta t} = S^n, \tag{49}$$

$$\Phi^{n+1} = \Phi^n + \Delta t S^n. \tag{50}$$

This method requires very small time steps, but on the other hand needs a very low mass storage.

5. NUMERICAL RESULTS

5.1. Evaporation of a falling droplet

Studying a falling droplet in an atmosphere at rest allows us to have values of the Sherwood and Nusselt numbers different from 2, as shown in Figure 2 for a falling drizzle droplet in an isothermal atmosphere. Corresponding to the very short acceleration phase of the droplet, we notice an increase in value of the Sherwood and Nusselt numbers up to their maximum value around 12. The following phase is relatively slow and marked by a linear decrease due to both falling drop ventilation and droplet evaporation.

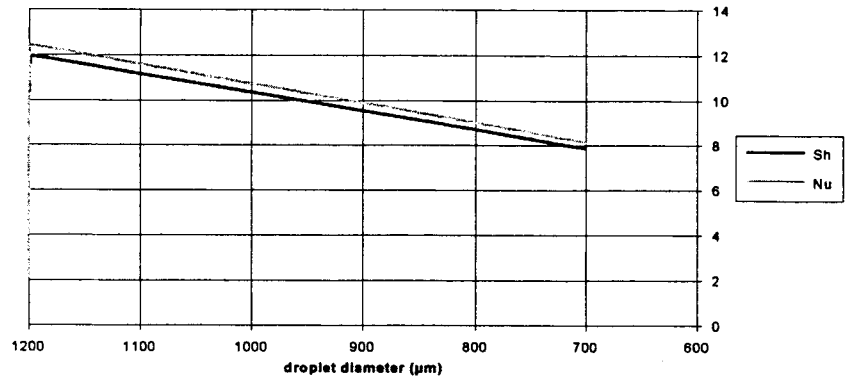

Figure 2. Evolution of Sherwood and Nusselt numbers during fall of 1200 μm initial diameter droplets

We consider two cases of falling croplet. In the first case we study the evaporation of a falling drizzle in a isothermal atmosphere (5 °C). The initial diameter is 1200 μm and the depth of fall is 2000 m. In the second case we determine the minimial value of the initial diameter for a droplet to survive a 300 m fall depth in a isothermal (0 °C) and isobaric (750 mbar) atmosphere. In both cases we compare our results with those of Beard and Pruppacher.[9]

In the first case the computation is performed for two saturation values, 80% and 40%. Figure 3 shows the results of the calculation and the comparison with Beard and Pruppacher's results. When the value of the saturation parameter is 80%, the curve resulting from our computation and that resulting from Beard and Pruppacher's computation are in good correspondence; the maximal difference is around 5%. However, when the value of the saturation parameter is 40%, our results tend to overestimate the droplet evaporation compared with those of Beard and Pruppacher; in this case the maximal difference is 23%.

In the second case we use only one value of the saturation, namely 90%. Figure 4 shows the comparison between Beard and Pruppacher's numerical results and our numerical results. From a qualitative point of view the two curves are in good correspondence and one may observe a quasivertical tangent at the start of both curves. However, from a quantitative point of view a discrepancy exists if we compare the values which build the curves: according to our calculation,

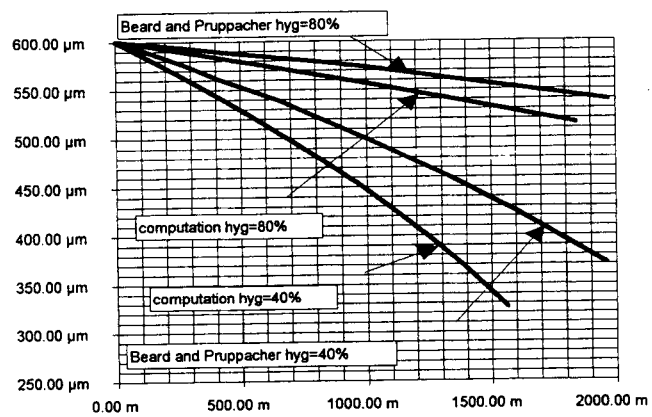

Figure 3. Evolution of a drizzle drop: comparison between Reference 9 and our computation

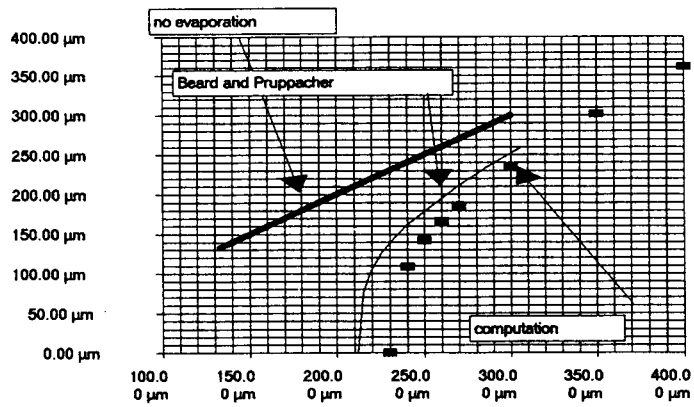

Figure 4. Final size of drops of various initial diameters in isothermal (0 °C) and isobaric (76.5 kPa) atmosphere (depth of the fall, 300 m)

the limiting diameter for whole droplet evaporation is 230 μm, instead of around 212 μm according to Beard and Pruppacher. The difference between the two calculations is 8.5%.

This difference results mainly from the assumption in our computation that the saturation remains constant around and in the vicinity of the droplet during its fall and so the quantity of water which becomes vapour does not alter the initial saturation value. Let us examine the influence of the vaporized water on the saturation value around the droplet. The saturation hg can be defined by

$$\rho_{v,real} = hg\rho_{v,sat}, \tag{51}$$

where $\rho_{v,real}$ is the density of water vapour when the partial pressure of vapour is equal to the saturation pressure and $\rho_{v,sat}$ is the density of water vapour around the droplet. Before the droplet fall (51) can be written as

$$\rho_{v,real,0} = hg_0\ \rho_{v,sat,0} \tag{52}$$

and during the fall at high y as

$$\rho_{v,real,y} = hg_y\ \rho_{v,sat,y}. \tag{53}$$

If we set the ratio hg_y/hg_0, we obtain

$$\frac{hg_v}{hg_0} = \frac{\rho_{v,sat,0}}{\rho_{v,sat,y}}\ \frac{\rho_{v,real,y}}{\rho_{v,real,0}}. \tag{54}$$

If the thermodynamic conditions remain constant around the droplet, we have $\rho_{v,sat,0}/\rho_{v,sat,y} = 1$ and (54) becomes

$$\frac{hg_y}{hg_0} = \frac{\rho_{v,real,y}}{\rho_{v,real,0}}. \tag{55}$$

We express (55) in terms of the water vapour mass by assuming that the water vapour is a perfect gas:

$$\frac{hg_y}{hg_0} = \frac{\rho_{v,real,y}}{\rho_{v,real,0}} = \frac{m_{v,y}}{m_{v,0}}. \tag{56}$$

Setting $m_{v,y} = m_{v,0} + \Delta m_{d,y}$, where $\Delta m_{d,y}$ is the water mass which becomes vapour when the droplet diameter drops from its initial value $d_{d,0}$ to the value $d_{d,y}$ at high y, we have

$$\frac{hg_y}{hg_0} = 1 + \frac{\Delta m_{d,y}}{m_{v,0}}. \tag{57}$$

In the case of droplet evaporation we have $\Delta m_{d,y} > 0$, so $hg_y > hg_0$; hence the value of the saturation increases in the vicinity of the droplet and the evaporation phenomenon tends to be slowed down. Keeping the saturation constant leads to an overestimation of the quantity of water which evaporates. According to relation (55), we also notice that keeping the saturation constant around and in the vicinity of the droplet means keeping the water vapour density constant too. Beard and Pruppacher[9] and Pruppacher and Klett[7] take into account the difference in vapour density between the vicinity and the environment to calculate the evolution of the diameter of a falling droplet, so the evolution of the saturation value in the vicinity of the droplet is taken into account implicitly.

Two reasons lead us not to adopt the Beard and Pruppacher modelling. First of all, the expression of droplet diameter evolution obtained in the case of a non-constant water vapour density introduces exponential calculations which will make the computation time long if we have to deal with numerous droplets. Secondly, in our domain of interest the distance within which we are studying droplet clouds is around 10 m and we can see in Figure 3 that the difference between Beard and Pruppacher's model and our model is almost negligible even at $y = 100$ m (for $hg = 80\%$ the difference is 0.3% and for $hg = 40\%$ the difference is 0.8%).

5.2. Evaporation of a polydisperse spray

In this subsection we consider a group of droplets with diameters in the approximate range from 5 to 60 μm. Each droplet is assumed to be injected into the flow with an initial velocity of 5 m s^{-1}. Figure 5 shows the evolution of the Reynolds number after injection for 10, 20 and 60 μm initial droplet diameters. The presented results have been computed with a constant aerodynamic velocity equal to 13 m s^{-1}.

Note that the value of the Reynolds number decreases very rapidly through a transient droplet motion corresponding to Sherwood and Nusselt numbers around 4 (i.e. high ventilation) to

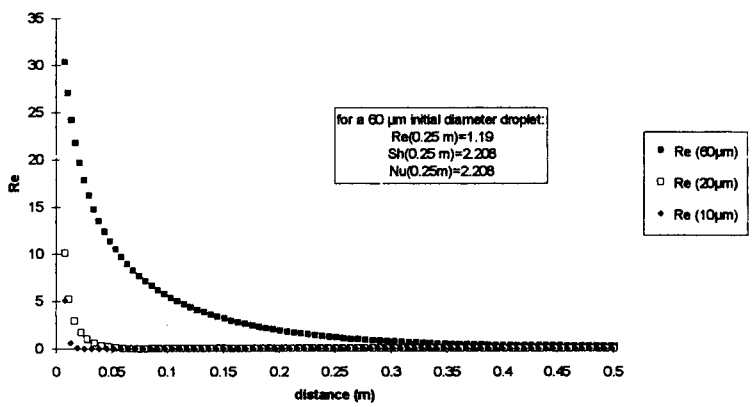

Figure 5. Evolution of Reynolds number for 10, 20 and 60 μm initial droplet diameters (gas velocity 13 m s^{-1}; initial droplet velocity 5 m s^{-1})

Table I. Aerodynamic conditions for granulometry measurements in a wind tunnel

Velocity (m s^{-1})	13·1
Averaged hygrometry (%)	45
Static temperature (°)	27
Turbulence rate (%)	1

reach a zero value corresponding to the steady state of the droplet motion, the Sherwood and Nusselt numbers then being equal or close to 2 (i.e. no ventilation). For a 20 μm droplet diameter the steady state flight is reached at $x = 0{\cdot}05$ m and for a 60 μm droplet diameter the same state is reached at $x = 0{\cdot}35$ m. However, if we postulate a 10% error in the value of the Sherwood and Nusselt numbers for no ventilation, it can be assumed that all droplets with a diameter within a range up to 60 μm have reached the steady state motion at 0·25 m.

Experimental data from granulometry measurements in a wind tunnel[26] have been obtained for a droplet cloud under the aerodynamic conditions summarized in Table I. The droplet cloud is obtained through a pneumatic nozzle. Two series of granulometry measurements are performed by means of a 'Malvern' device. The first and second series of measurements were performed at 0·25 and 1·95 m respectively from the spray outlet. We quantify the evaporation of the droplets between 0·25 and 1·95 m through the median volumic diameter (MVD). The values of the investigated MVD are 13·64, 17·49, 25·50, 33·80 and 40·21 μm with *diameters* ranging from about 5 to 60 μm. Numerically we use a classical turbulent profile to simulate the wind tunnel air flow. The cubic spline interpolation method is used to calculate the MVD value from the mass distribution of droplets per class of dimeter.[27] The MVDs obtained from measurements have been recalculated by mean of cubic splines to allow a coherent comparison between numerical and experimental results. All droplets are assumed to have the same speed as the flow when injected and their initial temperature is 15 °C. The value of the time step for Euler integration is 5×10^{-6} and the number of time steps is 31,000. Every run lasts around 3 h on a SUN/SPARK IPX workstation. In Figure 6 we follow the evaporation of droplets for

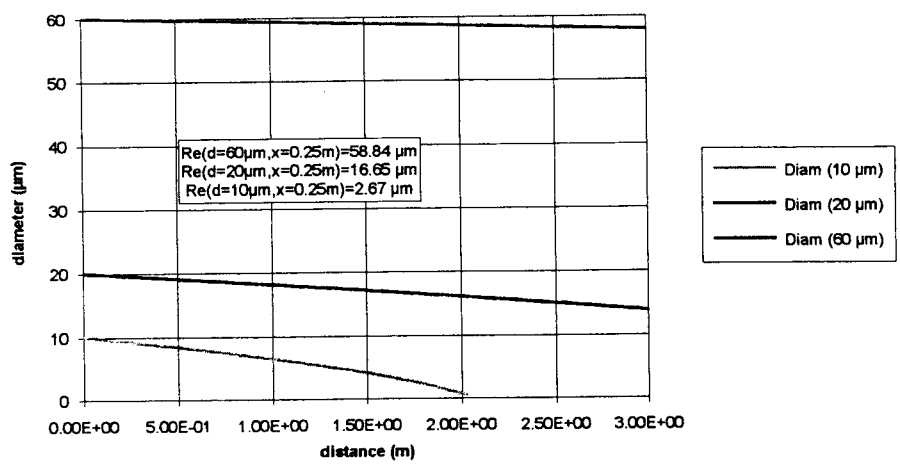

Figure 6. Evolution of droplets of 10, 20 and 60 μm initial diameters (velocity of aerodynamic flow, 13·1 m s^{-1}; saturation 42%; velocity of injection, 5 m s^{-1})

Table II. Comparison between numerical and experimental data. The results in columns (1) and (2) are calculated by means of a cubic spline method from experimental data

$x = 0{\cdot}25$ m measurement (1) (μm)	$x = 1{\cdot}85$ m measurement (2) (μm)	$x = 1{\cdot}95$ m computation (3) (μm)	Difference ((2) − (3))/2 (%)
13·38	18·46	19·80	7·26
18·18	23·44	22·61	3·54
25·28	30·30	30·73	1·42
32·56	38·82	38·04	2·01
41·01	45·50	45·72	0·48

10, 20 and 60 μm initial droplet diameters. Note that small-diameter droplets are very sensitive to the saturation conditon and are evaporated within 2 m of injection. We deduce that between 0·025 and 1·95 m the DVM of the cloud tends to increase.

This phenomenon is confirmed by experimental data which are presented together with the numerical data in Table II. It can be seen that the difference between computational and experimental data is within 8% for low MVD values (around 13 μm) and within 4% for MVD values greater than 18 μm.

We notice that the difference is rather high for low MVD values and decreases as the MVD value increases. This phenomenon is not significant, since the difference is within experimental uncertainty. We can consider that the experimental data and computational results are in good agreement.

6. CALCULATION IN REALISTIC GEOMETRY

We present a computation of the evolution of a droplet cloud considering a realistic geometry. This geometry is representative of a test cell with a helicopter air intake as the test object inside. The helicopter air intake is equpped with its turboshaft engine. A previous study[28] shows that high-diameter droplets are breathed by the engine in spite of their high inertia. In this section we are interested in the determination of the characteristics of the droplet cloud in the vicinity of the test object.

6.1. Spatial discretization

To take into account a complex geometry, we define a mesh on the rectangular domain $(x_a, y_a) \times (x_b, y_b)$ which includes the geometry concerned as

$$x_{i,i=1,\ldots,n}/ \quad x_1 = x_a, \quad x_n = x_b, \quad x_{i-1} \leq x_i \leq x_{i+1},$$

$$x_{j,j=1,\ldots,m}/ \quad y_1 = y_a, \quad y_m = y_b, \quad y_{j-1} \leq y_j \leq y_{j+1}.$$

We relate each node to a node function $\Im_{i,j}$ in fact an 'impermeability' function, defined as

$$\Im(x_i, y_j)_{i=1,\ldots,n;\, j=1,\ldots,m} = \Im_{i,j} = \{0; 1; 2; 3; 4; 5; 6; 7; 8; 9; 10\}.$$

The value of the function $\Im_{i,j}$ depends on the location of the node: 0-value is for the computable part of the domain and 10-value is for the non-computable part. Intermediate values from 1 to

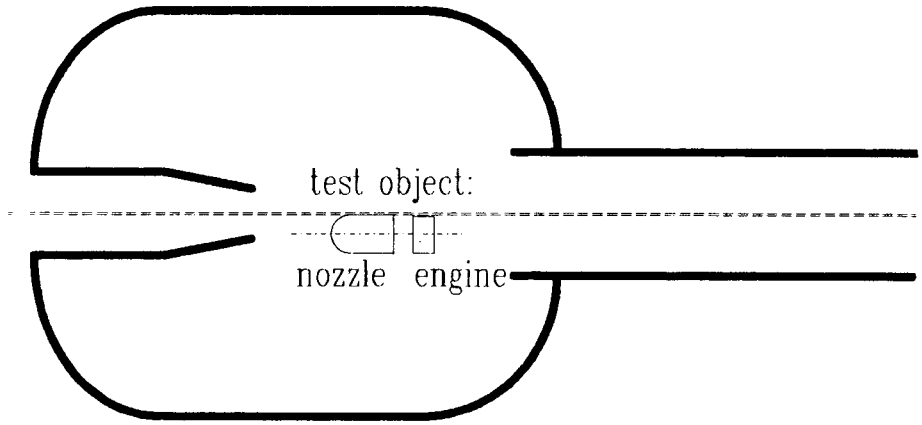

Figure 7. Geometry of test problem

4 are for nodes in the vicinity of walls and values from 5 to 8 are nodes located at corners. Thus we are able to recognize the inner limits of the obstacles and we can impose appropriate boundary conditions for velocity and pressure field calculation. If $\Im_{i,j} = 9$, we impose the velocity on the node. This possibility is used when a simulation of an engine run is required. The main advantages of such a method are its simplicity and its great adaptability. However, in the case of a very complicated geometry the ratio of the number of nodes in the non-computable part of the domain to the number of nodes in the computable part may be quite important. As a result, the time spent on useless nodes may be not negligible. Another advantage of the method in our case is that the function $\Im_{i,j}$ can be used to calculate whether a droplet is in the vicinity of a wall or not, as we will see later.

Equations (41), (42) and (46) are discretized by means of a classical finite difference method on a staggered marker-and-cell (MAC) mesh introduced by Harlow and Welch.[29] A second-order 'power law' scheme[30] which takes into account the local characteristics of the flow is used for the convective term discretization and a centred second-order scheme is used for the diffusive term discretization. The resulting linear systems are solved through a preconditioned conjugate gradient method.[31]

The computation is carried out on the geometry shown in Figure 7. We choose to have an extended exhaust in order to minimize the effect of the outflow boundary conditions on the upstream recirculation zones. A uniformly distributed mesh is used across the domain. The number of nodes is 219 in the flow direction and 191 in the transverse direction. The ratio of non-computable nodes to computable ones is about 0·3.

6.2. Numerical run conditions and results for aerodynamic flow

The projection method described in the set of equations (41)–(47) is not time-accurate enough to be used for unsteady phenomena.[32,33] We use time marching only to reach an approximation of a steady state solution of (41)–(47). In that case the steady state solution is regarded as an asymptotic limit of a time progression.

The calculations are carried out at a Reynolds number of 10^6 and a Mach number of 0·2. The Reynolds number is based on the end diameter of the Mach nozzle. To have a divergence-free velocity field for the first time step, the potential flow is used on initial solution. The value of

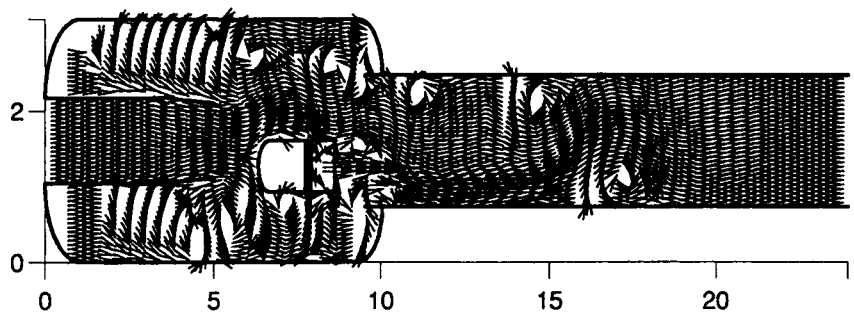

Figure 8. Result of air flow computation

the time step is 0·02. We stop the computation when we detect no significant evolution of the velocity at the entrance of the exhaust and this state corresponds to a dimensionless time value of 40. The computation time is 40 min on the CRAY YMP of ONERA and the mean value of the velocity divergence is around 10^{-3}.

The result of the aerodynamic computation is shown in Figure 8.

6.2.1 Initial conditions for two-phase calculation. To be able to calculate the evolution of water droplets in the aerodynamic flow through equations (11), (29), (39) and (40), we need to know the temperature field and the saturation field. As a matter of fact, the quantity x_v related to a droplet in equation (16) has the definition

$$x_v = hg \frac{e_w(T)}{p},$$

where hg is the saturation of the flow around the droplet, T is the static temperature, p is the static pressure and $e_w(T)$ is the saturation pressure related to the temperature T. We define the saturation hg as

$$hg = \Re \frac{p}{e_w(T)}, \tag{58}$$

with

$$0 \leq hg \leq 1,$$

where $\Re$ is a constant which depends mainly on the supersaturation temperature. On every node $(i, j)_{i=1,\ldots,n;\, j=1,\ldots,m}$ of the previously defined mesh we write (58) as

$$hg_{i,j} = \Re \frac{p_{i,j}}{e_w(T_{i,j})}\bigg|_{i=1,\ldots,n;\, j=1,\ldots,m} \tag{59}$$

On a wall we impose $hg|_{wal} = 1$ if condensation occurs. To calculate the constant $\Re$, we assume the saturation, static pressure and static temperature to be knonw as (x_0, y_0), then we can write

$$\Re = \frac{hg_{x_0,y_0} e_w(T_{x_0,y_0})}{p_{x_0,y_0}}. \tag{60}$$

In our case we have $h_0 = 95\%$, $T_0 = -5\,^{\circ}\mathrm{C}$ and $p_0 = 80{,}000$ Pa. The location of (x_0, y_0) is at the exit of the Mach nozzle and on the symmetry axis. For our computation we assume for the temperature $T = T_0$ all over the computational domain.

Table III. Initial mass distribution of droplets as a function of diameter for a DVM value of 25·15 μm

Diameter (μm)	Percentage of mass
5·80	4·73
7·20	2·41
9·10	3·42
11·40	4·02
14·50	7·65
18·50	8·96
23·70	14·80
30·30	17·22
39·00	19·33
50·20	15·91
64·60	1·55

At each time step and for each droplet the gas velocity, saturation and temperature at the location of the droplet are calculated through a bilinear interpolation from the values of the corresponding fields at the four nodes in the vicinity of the droplet location.

For the spray we consider a 25·15 μm MVD cloud and we present the mass distribution in Table III.

To introduce droplets in the aerodynamic flow, we define a rectangular area located at the entrance of the geometry and inside the Mach nozzle. Inside this injection area the location of each injected droplet is calculated through a random function. All droplets have the same injection velocity (5 m s^{-1}) and injection temperature (T_d = 15 °C). The spray is composed of about 1100 droplets. The time step value for Eulier integration is 10^{-6} and the number of steps is 10,000. A run lasts around 1 h on a SUN/SPARK IPX workstation.

6.2.2. Numerical results for droplet spray. Figures 9–11 show the cloud computed at three important locations, first at the exit of the Mach nozzle, second when impacting the obstacle and third near the air intake. During the cloud motion in the Mach nozzle the important environment saturation (around 93%) causes no noticeable evolution of the characteristics of the cloud and in particular the MVD remains constant. Near the leading edge of the obstacle we have to deal with the problem of the determination of impacting droplets. To calculate the trajectory of a droplet in the vicinity of a wall, we need to know the aerodynamic flow field near the wall and then we have to calculate the boundary layer accurately. In our case we do not have enough nodes near the obstacle walls to compute the boundary layer, but we are able to know whether a droplet is in the vicinity of a wall by means of the function $(\Im_{i,j})_{i=1,\ldots,n;\, j=1,\ldots,m}$ defined in Section 6.1. As a matter of fact, if we suppose a droplet location to be

$$(x_d, y_d)_{i_d, i_d = 1, \ldots, n_d},$$

where n_d is the number of droplets in the cloud, $(x_d, y_d)_{i_d}$ belongs to the node $(x_i, y_j)_{i=1,\ldots,n;\, j=1,\ldots,m}$ defined as

$$x_i \leq x_d \leq x_{i+1}, \qquad y_j \leq y_d \leq y_{j+1}.$$

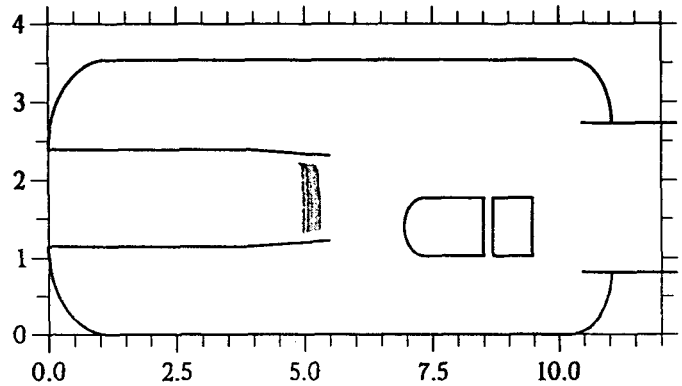

Figure 9. Spray at end of convergent nozzle

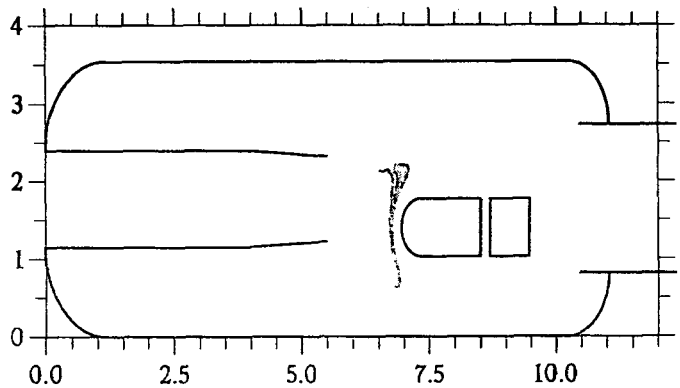

Figure 10. Spray impacting leading edge of obstacle

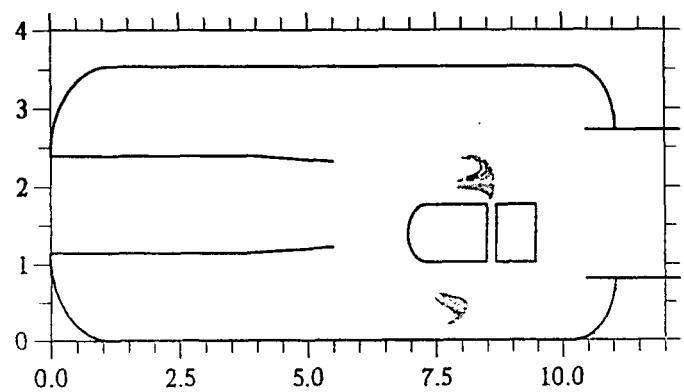

Figure 11. Spray breathed by engine through air intake

Table IV. Evolution of ratio $r_{\zeta,iclass}$

Class of diameter (μm)	Ratio $r_{\zeta,iclass}$ (%)
5·80	3·60
7·20	6·00
9·10	3·20
11·40	7·60
14·50	7·20
18·50	7·20
23·70	10·40
30·30	8·80
39·00	14·00
50·20	13·20
64·60	18·80
Impact < 30 μm	45·20%
Impact > 30 μm	54·80%
'Vicinity' MVD	27·3 μm

We define the following summation on the node $(x_i, y_j)_{i=1,\ldots,n;\ j=1,\ldots,m}$

$$\zeta_{i,j} = \sum_{\substack{k=0,1 \\ l=0,1}} \Im_{i+k,j+l}. \tag{61}$$

The droplet is in in the vicinity of the wall when

$$\zeta_{i,j} > 10 \tag{62}$$

It can be noticed that the 'vicinity function' to be computed once and for all before carrying out the droplet evolution computation. In the case of a front impact we assume that all the droplets located in the vicinity of the wall are droplets which will impact the wall. Thus we can calculate the number of droplets which have a high probability of bumping into the obstacle on the leading edge but we cannot determine the location of the impacts. In Table IV we report the value of the ratio

$$r_{\zeta,iclass} = \left.\frac{m_{\zeta,iclass}}{m_{0,iclass}}\right|_{iclass=1,\ldots,nclass} \tag{63}$$

where $n$class is the number of classes of droplet diameter in the cloud, $m_{\zeta,iclass}$ is the mass in the vicinity of the obstacle related to the class number $i$class and $m_{0,iclass}$ is the initial mass of droplets related to the class number $i$class for each class of droplet diameter in the cloud.

The droplets are almost equally distributed among low-diameter droplets ($d < 30$ μm) and high-diameter droplets ($d > 30$ μm), with a slight advantage for low-diameter droplets. The local ('vicinity') MVD is assessed to be 27·3 μm, which is of the same order of magnitude as the initial cloud MVD (27·115 μm). If we assume that all the droplets in the vicinity of the leading edge are impacting droplets, but on the other hand we suppose that an impacting droplet vanishes, we can calculate that the MVD of the cloud far from the wall jumps from 25·15 to 23·9 μm.

Near the air intake we define a local rectangular area Ω_{screen} as follows: length, 1 m centred on the aperture of the air intake; height, 5 cm from the wall. These dimensions correspond to the usual location of an air intake screen on a helicopter test object. We pay some attention to determine first the 'air intake' MVD, which is related to the droplets inside the previously defined

Table V. Droplets breathed through air intake

Class of diameter (μm)	Percentage breathed by air intake
5·80	11·21
7·20	10·57
9·10	11·52
11·40	10·25
14·50	10·25
18·50	9·62
23·70	8·88
30·30	8·88
39·00	7·08
50·20	6·66
64·60	5·07
Impact < 30 μm	72·30%
Impact > 30 μm	27·70%
'Incoming' MVD	13·35 μm

are Ω_{screen}, and second the 'incoming' MVD, which characterizes the droplets breathed by the engine through the air intake (Table V).

For the nodes which belong to Ω_{screen} we set

$$\Im(x_i, y_j)_{(x_i, y_j) \in \Omega_{\text{screen}}} = 11, \tag{64}$$

where $\Im(x_i, y_j)$ is the node function previously defined. From equations (64) and (61) we obtain the relation

$$\zeta_{i,j}|_{i=1,\ldots,n;\ j=1,\ldots,m} = 44 \quad \Leftrightarrow \quad (x_i, y_j)_{i=1,\ldots,n;\ j=1,\ldots,m} \in \Omega_{\text{screen}}. \tag{65}$$

By testing the value of $\zeta_{i,j}$ at each time step, it is easy to know whether a droplet is in the domain Ω_{screen} or out of the domain Ω_{screen}, since at each time step we can determine the mass distribution of the cloud inside the domain Ω_{screen} and the corresponding MVD. the final 'air intake' MVD is the result of a time average.

The value computed for the 'air intake' MVD is 18·74 μm. The difference between this and the MVD of the cloud far from the wall is significant (21%) and we are led to think that high-diameter droplets tend to remain far from the area concerned because of their momentum. This phenomenon is emphasized for the droplets breathing in the air intake. The incoming MVD value is 13·35 μm and by computing the ratio (63) on the domain Ω_{screen}, it can be noted that 72% of the engine-breathed droplets have a diameter smaller than 30 μm (Table V).

7. CONCLUDING REMARKS

To compute the evolution of a water droplet spray inside a complex geometry requires two main points. First we have to take into account the obstacles located in the flow. Second, if we consider the droplets of the spray capable of evaporation, we need to have exchange laws related to mass and heat transfer for the droplets.

In our case the mass and heat transfer laws are deduced from the definition of the heat and mass coefficients and we assume that in the vicinity of the droplet the quantity of vapour in the air remains constant during the whole computation. This assumption leads to important differences between our numerical results and the literature results in the case of a distance of computation

around 1000 m. However, in our domain of interest the distance of computation does not exceed 10 m and in this case the results obtained from our modelling are very close to the literature results. Our results are also close to experimental data obtained from granulometry measurements in a wind tunnel.

In the case of a complex geometry we introduce a function related to the nodes which separates the nodes into two groups, a computable one and a non-computable one. Thus we are easily able to take into account the obstacle in the flow for the gas flow computation and for the droplet trajectory calculation too. In the case of a realistic geometry we are able to follow each droplet of the spray and determine the local characteristics of the spray in the vicinity of the wall of the obstacle.

ACKNOWLEDGEMENTS

The author is grateful to J. L. Guermond, D. Guffond, R. Henry, A. Lasek and F. Feuillebois for their helpful remarks on this work.

REFERENCES

1. G. M. Faeth, 'Evaporation and combustion of a spray', *Prog. Energy Combust. Sci.*, **9**, 1–76 (1988).
2. G. M. Faeth, 'Current status of droplet and liquid combustion', *Prog Energy Combust. Sci.*, **3**, 191–224 (1977).
3. W. A. Sirignano, 'Fuel droplet vaporization and spray combustion theory', *Prog. Energy Combust. Sci.*, **9**, 291–332 (1983).
4. W. A. Sirignano, 'An internal approach to spray combustion model development', *Combust. Sci. Technol.*, **58**, 231–251 (1988).
5. C. K. Law, 'Recent advances in droplet vaporization and combustion', *Prog. Energy Combust. Sci.*, **8**, 171–201 (1982).
6. G. L. Hubbard, V. E. Denny and A. F. Mills, 'Droplet evaporation: effects of transients and variable properties', *Int. J. Heat Mass Transfer*, **18**, 1003–1008 (1975).
7. H. R. Pruppacher and J. Klett, *Microphysics of Clouds and Precipitation*, Reidel, Dordrecht, 1978.
8. N. H. Fletcher, 'The freezing of water', *Sci. Prog.*, **54**, 227–241 (1966).
9. K. V. Beard and H. R. Pruppacher, *J. Atmos. Sci.*, **28**, 1455 (1971).
10. Fueillebois, Lasek, P. Creismeas, Pigeonneau and A. Szaniawski, 'Freezing of a subcooled liquid droplet', *J. Colloid. Interface* (1994) (in press).
11. G. Gouesbet, P. Desjonquieres and A. Berlement, 'Eulerian and Langrangian approaches to turbulent dispersion of particles', *Proc. Int. Seminar on Transient Phenomena in Multiphase Flow*, Durbovnik, May 1987.
12. F. Durst, 'Eulerian and Lagrangian predictions of particulate two-phase flows: a numerical study', *Appl. Math. Modell.*, **8**, 101–114 (1984).
13. A. A. Mostafa and H. C. Mongia, 'On the modelling of turbulent evaporation sprays: Eulerian versus Lagrangian approach', *Int. J. Heat Mass Transfer*, **30**, 2583–2593 (1987).
14. A. Adeniji-Fashola and C. P. Chen, 'Modelling of confined turbulent fluid particle flows using Eulerian and Lagrangian schemes', *Int. J. Heat Mass Transfer*, **33**, 691–701 (1990).
15. A. C. Benim and Neuhoff, 'Analysis of erosion behavior in a turbo charger radial turbine', *Int. J. Numer. Methods Fluids*, **16**, 259–285 (1993).
16. G. M. Faeth, 'Mixing transport and combustion in sprays', *Prog. Energy Combust. Sci.*, **13**, 293–345 (1987).
17. K. -C. Chang, M. -R. Wang, W. -J. Wu and Y. -C. Liu, 'Theoretical and experimental study on two-phase structure of planar mixing layer', *AIAA J*, **31**, (1993).
18. C. T. Crowe, J. N. Chung and T. R. Troutt, 'Particle mixing in free shear flows', *Prog. Energy Combust. Sci.*, **14**, 171–194 (1987).
19. J. Courquet, 'Mise au point d'une méthode de décomposition d'un écoulement en foyers élémentaires à partir d'un calcul complet', *Thèse de Docteur*, Université Paul Sabatier, Toulouse, 1991.
20. J. K. Dukowicz, 'A particle–fluid numerical model for liquid spray', *J. Comput. Phys.*, **35**, 229–253 (1980).
21. C. E. Willbanks and R. J. Schulz, 'Analytical study of icing simulation for turbine engine in altitude test cells', *AEDC-TR73-144*, 1973.
22. O. Metais and M. Lesieur, 'Spectral large eddy simulation of isotropic and stably stratified turbulence', *J. Fluid Mech.*, **239**, 157–194 (1992).
23. J. Smagorinsky, *Mon. Weather Rev.*, **91**, 99–164 (1963).
24. A. Chorin, 'Numerical simulation of the Navier–Stokes equations', *Math. Comput.*, **22**, 745–762 (1968).
25. R. Temam, 'Une méthode d'approximation de la solution des équations de Navier–Stokes', *Bull. Soc. Math. Fr.*, **98**, 115–152 (1968).

26. P. Creismeas and J. Courquet, 'Modélisation numérique de l'évolution d'un nuage de gouttelettes d'eau en surfusion dans un caisson givrant', *AGARD CPP*, **480**, (1990).
27. J. H. Ahlberg, E. N. Nilson and J. L. Walsh, *The Theory of Splines and Their Applications*, Academic, New York, 1969.
28. P. Creismeas and J. Courquet, 'Numerical prediction of an icing cloud; application to the determinatin of diphasic characteristics of a spray in the neighbourhood of a turboshaft in icing test', *Proc. 10th ISABE Symp.*, Nottingham, 1991.
29. F. H. Harlow and F. E. Welch, 'Numerical calculation of time-dependent viscous incompressible flow of fluid with free surface', *Phys. Fluids*, **8**, 2182–2189 (1965).
30. M. K. Patel and C. M. Markatos, 'Evaluation of height discretization schemes for two-dimensional convection–diffusion equations', *Int. j. numer. methods fluids*, **6**, (1986).
31. M. Zedan, 'A coupled strongly implicit procedure for velocity and pressure computation in fluid flow problems', *Numer. Heat Transfer*, **8**, (1981).
32. J. Shen, 'On error estimates of projection methods for Navier–Stokes equations: first-order schemes', *SIAM J. Numer. Anal.*, **29**, 57–77 (1992).
33. J. L. Guermond, 'Some error estimates for the approximation of the unsteady Navier–Stokes equations by means of projection methods', *SIAM J. Numer. Anal.*, (in press).